

Article

Two-Dimensional Iron Phosphorus Trisulfide as a High-Capacity Cathode for Lithium Primary Battery

Syama Lenus^{1,2}, Pallavi Thakur², Sai Smruti Samantaray², Tharangattu N. Narayanan^{2,*} and Zhengfei Dai^{1,*} ¹ State Key Laboratory for Mechanical Behavior of Materials, Xi'an Jiaotong University, Xi'an 710049, China² Tata Institute of Fundamental Research, Hyderabad 500046, India

* Correspondence: tnn@tifrh.res.in (T.N.N.); sensdai@mail.xjtu.edu.cn (Z.D.)

Abstract: Metal phosphorus trichalcogenide (MPX₃) materials have aroused substantial curiosity in the evolution of electrochemical storage devices due to their environment-friendliness and advantageous X-P synergic effects. The interesting intercalation properties generated due to the presence of wide van der Waals gaps along with high theoretical specific capacity pose MPX₃ as a potential host electrode in lithium batteries. Herein, we synthesized two-dimensional iron thio-phosphate (FePS₃) nanoflakes via a salt-template synthesis method, using low-temperature time synthesis conditions in single step. The electrochemical application of FePS₃ has been explored through the construction of a high-capacity lithium primary battery (LPB) coin cell with FePS₃ nanoflakes as the cathode. The galvanostatic discharge studies on the assembled LPB exhibit a high specific capacity of ~1791 mAh g⁻¹ and high energy density of ~2500 Wh Kg⁻¹ along with a power density of ~5226 W Kg⁻¹, some of the highest reported values, indicating FePS₃'s potential in low-cost primary batteries. A mechanistic insight into the observed three-staged discharge mechanism of the FePS₃-based primary cell resulting in the high capacity is provided, and the findings are supported via post-mortem analyses at the electrode scale, using both electrochemical- as well as photoelectron spectroscopy-based studies.

Keywords: metal phosphorus trichalcogenides; discharge mechanism; cathode electrolyte interface; lithium primary battery



Citation: Lenus, S.; Thakur, P.; Samantaray, S.S.; Narayanan, T.N.; Dai, Z. Two-Dimensional Iron Phosphorus Trisulfide as a High-Capacity Cathode for Lithium Primary Battery. *Molecules* **2023**, *28*, 537. <https://doi.org/10.3390/molecules28020537>

Academic Editors: Shijun Liao, Xiangbo Meng, Yuanfu Deng and Xiaoyuan Zeng

Received: 24 November 2022

Revised: 25 December 2022

Accepted: 29 December 2022

Published: 5 January 2023



Copyright: © 2023 by the authors. Licensee MDPI, Basel, Switzerland. This article is an open access article distributed under the terms and conditions of the Creative Commons Attribution (CC BY) license (<https://creativecommons.org/licenses/by/4.0/>).

1. Introduction

With an energy density of nearly 500 Wh Kg⁻¹, primary batteries practically possess higher energy density and have greater long-run capability than secondary batteries, which possess low gravimetric energy density values of ~150–200 Wh Kg⁻¹ [1]. In light of the plethora of applications spanning from disposable electronics to the mining industry, defense forces, aerospace technology, and medical fields, primary batteries represent a major part of the battery industry, similar to secondary (mostly Li-ion) batteries [2–4]. Among the lithium primary batteries, the fluorinated graphene (Li/CF_x)-based batteries with a theoretical capacity of 865 mAh g⁻¹ are well-studied, commercially available, and are the most popularly reported systems [5,6]. However, a few reports also emphasize that fluorocarbons, in which the carbon is bound to fluorine, are potent greenhouse gases on degradation (recycling), and some form toxic compounds that can accumulate in the environment [7]. Furthermore, neutralizing the fluorocarbons requires a process that includes high temperature, which drives up its cost and thus limits its adoption [7]. Additionally, CF_x-based primary batteries are accompanied by intrinsic disadvantages that include low discharge voltage platform, inadequate rate performance, and voltage hysteresis accompanied by a severe exothermic phenomenon [8–10]. Researchers have also explored the other possible lithium primary batteries; however, most among those are extremely toxic and corrosive and pose harsh safety concerns [11]. Other materials for LPBs mainly include copper vanadate (CuV₂O₆) [12], silver vanadium oxide (Ag₂V₄O₁₁) [13], aluminum fluoride (Li/AlF₃) [2], and manganese dioxide (Li/MnO₂) [14] with layered

structures. However, unfortunately, the multistep reductions that occur during the insertion/intercalation of lithium in these materials results in their low specific capacity [15]. Two-dimensional metal chalcogenides (2DMCs) with carbon are a well-studied system for lithium batteries [16]. Moreover, the need for proficient energy consumption makes eco-friendly, non-carbonaceous materials more attractive and demanding.

Interestingly, when investigating the long history of 2DMCs, it was found that layered metal phosphorus trichalcogenides MPX_3 (where M = transition metals, X = S, Se) have magnificent characteristics including exceptional intercalation characteristics and tunable bandgaps for electrochemical storage applications [17,18]. Indeed, as an anode material in LIB, MPS_3 has a high value of theoretical capacity ($>1000 \text{ mAh g}^{-1}$), with the Li binding energy value being greater than $\sim 1.7 \text{ eV}$, thus eliminating the possibility of dendrite growth. For instance, Datta et al. [19] reported the lithium ion binding energies on all the $TMPs_3$ monolayers as -2.03 , -2.31 , -1.71 , and -2.29 eV for the transition metals, TM = Mn, Fe, Co, and Ni, respectively, specifying the low possibility of Li clustering. Among all these, $FePS_3$ can be a highly efficient candidate due to the presence of the most abundant TM, i.e., iron (Fe), as the constituent. Moreover, it has been explored as an electrode for lithium metal batteries at low current values [20]. In many applications, such as pacemakers, toys, devices used in military/rescue missions, etc., the use of a secondary Li battery, given their shorter discharge time, is non-recommended. Thus, it is of high significance to pursue new environmentally benign electrode materials for LPBs that could provide high energy density at lower cost. As mentioned, $FePS_3$ is an ideal candidate from the $TMPX_3$ family, which holds an octahedral structure that could primarily incorporate Li ions following a two-electron transfer during the reduction of Fe^{2+} to Fe^0 [21,22]. However, research on $FePS_3$ as an electrode material in LPB is still in its infant stage, predominantly due to its harsh and long-term solid-reaction synthesis protocol [23,24]. Hence, we made efforts in this direction by focusing on the development of a facile synthesis method for 2D $FePS_3$ and understanding its properties for its application in a LPB at high current density.

Herein, we report the use of iron thiophosphate ($FePS_3$), synthesized via a salt-template method, as an efficient lithium primary battery electrode that can deliver a high specific capacity (1791 mAh g^{-1}) and energy density (2500 Wh Kg^{-1}). An insight into the discharge mechanism is put forward through ante-/post-battery discharge results. Differing from its reversible behavior within the range of 1 V vs. Li/Li^+ , $FePS_3$ demonstrates an irreversible discharge behavior beyond 1 V. In this work, we methodically scrutinize the capacity enhancement of the system at different voltages using various electrochemical and spectroscopic techniques. The discharge mechanism is explained as a three-stage mechanism. It is revealed here, for the first time, that the presence of defect centers and the formation of a CEI (cathode–electrolyte interface) layer eventually led to the high capacity exhibited during the first and third stages of the discharge process, respectively, while the second stage can be attributed to the lithiation in the $FePS_3$ layers. Even at the high discharge current density value of 1 A g^{-1} , the $FePS_3$ -based LPB delivers a specific capacity of 867 mAh g^{-1} , which is still higher than the other reported systems, such as CF_x and $FePS_3$ (previous reports), which were discharged at lower current density values. This study unravels the possibility of achieving high-capacity, affordable, and environment-friendly electrodes-based next-generation LPBs using $FePS_3$ cathode materials.

2. Results

2.1. Synthesis of $FePS_3$ Nanoflakes

Salt-template synthesis [24] can be considered as a nearly ideal synthesis strategy to prepare the compounds of MPX_3 family because of its simplicity, low cost, low temperature, ambient growth conditions, and less time required to obtain well-grown crystals compared to the time taken with other existing synthesis methodologies. Therefore, a similar approach was adapted to synthesize the two-dimensional layered $FePS_3$ using sodium chloride (NaCl) as a soft template, as shown in the Figure 1a (details are mentioned in Section S1, Electronic Supplementary Information (ESI)). The formation of $FePS_3$ on the surface of the NaCl

template takes place in a nitrogen atmosphere within a duration of 16 h. During the initial stages of synthesis, i.e., at 310 °C, the formation of FeS_x and P_xS_y moieties takes place, as confirmed by X-ray photoelectron spectroscopic (XPS) studies given in the ESI. Further, yet another XPS study was conducted at the initial stage of synthesis of FePS_3 at 310 °C (Figure S6.5), where a high amount of S, FeS_x , and P_xS_y were observed, and peaks corresponding to FePS_3 were absent. Additional information with XPS spectra (Figure S6.5, Section S6) is provided in the Supplementary Information. Eventually, when the temperature further rises to 500 °C, these FeS_x and PS_y moieties react to form the final product FePS_3 . The transformation can also be realized through the color change, where the dark brown mixture of FeCl_3 -coated NaCl well-ground with sulfur and phosphorus powder turns into a black-colored FePS_3 powder after the furnace treatment (shown in ESI, Figure S1).

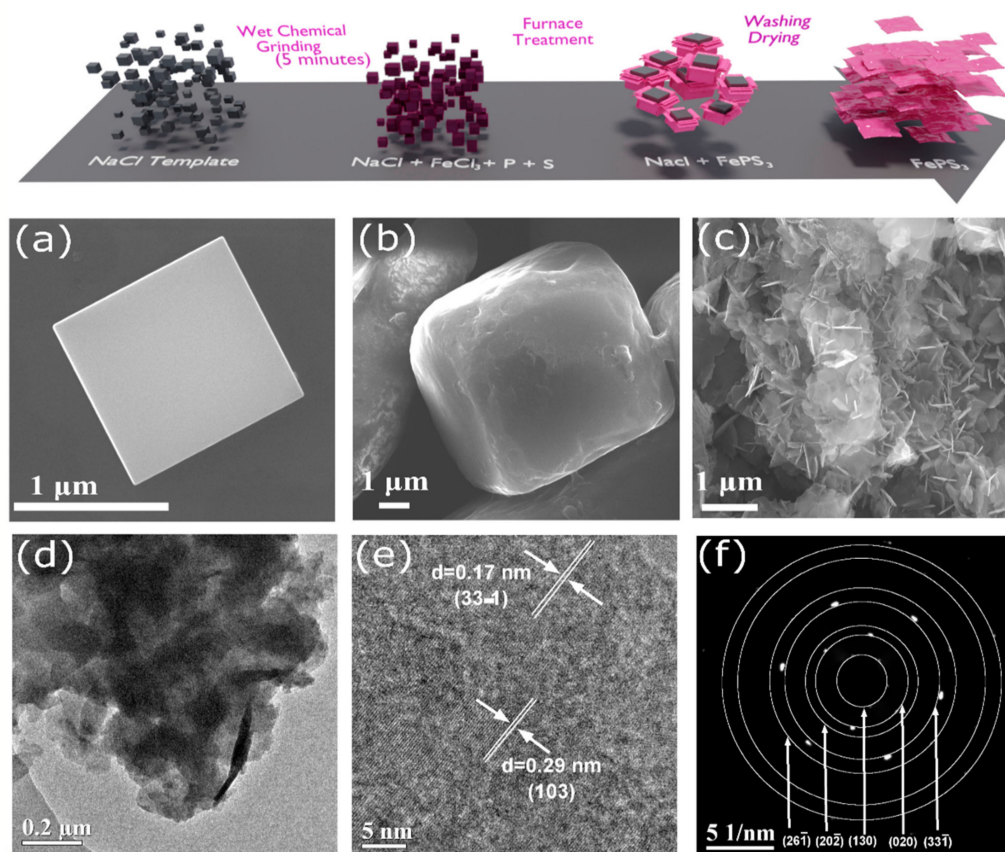


Figure 1. Schematization of the synthesis strategy of FePS_3 via the salt-template method. SEM images of (a) NaCl template (b) FeCl_3 , sulfur, and phosphorus-coated NaCl and (c) FePS_3 nanoflakes. (d) TEM image of FePS_3 nanoflakes; (e) HRTEM image of a representative FePS_3 . The well-defined interlayer spacing of 0.17 and 0.29 nm indicates the presence of crystalline FePS_3 . (f) Selected area electron diffraction (SAED) pattern of FePS_3 nanoflakes.

2.2. Characterisation of FePS_3 Nanoflakes

The surface morphology of the FePS_3 nanoflakes was analyzed by field-emission scanning electron microscopy (FE-SEM). The FE-SEM images of the samples at the different stages of synthesis are shown in Figure 1b–d. The NaCl template cubes (Figure 1b) are conformally coated with the mixture of FeCl_3 , sulfur, and phosphorus (Figure 1c). The morphology of FePS_3 disclosed a dense cluster of nanoflakes having an average thickness of 35 nm and average areal dimensions of 350 nm, respectively. Indeed, the growth of nanoflakes on the NaCl template occurred in a stacked manner, wherein more than five nanoflakes grow on top of the FePS_3 nanoflakes, as can be seen in the SEM images (Figure S2b ESI). Further, the SEM images of FePS_3 nanoflakes at different magnifications are given in Figure S2a–c. As shown in the SEM images (Figure S2d,e), when large-sized

(>10 μm) NaCl crystals were used as the templates, we obtained nanosheets of FePS_3 compared to the nanoflakes obtained when the smaller-sized ($\sim 1 \mu\text{m}$) NaCl template was used. The nanoflakes could provide more active edges and surface area for lithium ion storage compared to the nanosheets; hence, they were chosen for the study. SEM-assisted energy dispersive X-ray spectroscopy (EDS) analysis was also performed on the as-synthesized FePS_3 nanoflakes. The elemental mapping confirms the presence of Fe, P, and S throughout the sample, with the relative atomic percentage being 1:1:3, as that in FePS_3 (Figure S3). The high-resolution transmission electron microscopy (HR-TEM) analysis of the FePS_3 sample confirms the flake-like morphology (Figure 1e). The interplanar spacing (d-spacing) of 0.29 and 0.17 nm correspond to (130) and (33 $\bar{1}$) crystal planes of FePS_3 (Figure 1f), respectively, which is further confirmed by the selected area electron diffraction (SAED) pattern (Figure 1g).

To confirm the crystal structure of the FePS_3 nanoflakes, the X-ray diffraction (XRD) pattern of the powder sample was analyzed (Figure 2a). The diffraction pattern consists of sharp peaks at 14° , 31° , 36° , and 54° that correspond to the (001), (130), (20 $\bar{2}$), and (33 $\bar{1}$) crystalline planes of FePS_3 with a monoclinic unit cell (ICSD No. 01-078-0496), which is accordance with the previous studies [25]. The miller indices (hkl) also match those obtained from the SAED pattern. Based on this information, the crystal structure (a representative structure without scaling) of the molecule is shown in the Figure 2a inset. The clear octahedral voids seen in the image would be the ideal free space for Li intercalation. The Raman spectra of FePS_3 (Figure 2b) exhibit all the characteristics peaks of FePS_3 , including three A_{1g} and three E_g modes along with one E_u mode; these are the commonly observed peaks in the Raman spectra of MPS_3 materials [24]. The A_{1g} and E_g peaks correspond to the in-plane and out-of-plane vibrations of the $\text{S}_3\text{P}-\text{P}_3\text{S}$ unit. Another fingerprint characterization is its magnetic properties, and they are analyzed using vibrating sample magnetometry (VSM) studies (Figure 2c). The details of the measurements are given in ESI Section S4. The study confirmed the Neel temperature of FePS_3 as 123 K (the details of the field cooling (FC) and zero field cooling (ZFC) measurements are given in the ESI), in agreement with previous studies [26]. Additionally, the thermogravimetric analysis (TGA) shows the thermal decomposition temperature of FePS_3 at around 550°C , in line with the reports [27].

The XPS survey spectrum of FePS_3 nanoflakes (Figure S6.1 ESI) also confirms the presence of Fe, P, and S in the synthesized FePS_3 sample, with no traces of NaCl left in the sample. The high-resolution core-level XPS spectra of Fe 2p (3/2), P 2p(3/2), and S 2p(3/2) are obtained at 712.02 eV, 132.8 eV, and 163.0 eV, respectively [28]. The atomic ratio of Fe:P:S calculated from the XPS spectrum was found to be 1:1:3, which is in agreement with the EDS findings and hence ensures the stoichiometry FePS_3 . The layered FePS_3 possess the same monoclinic structure as that of CdX_2 ($X = \text{Cl}, \text{I}$) where the metallic centers are replaced by Fe^{2+} and P-P (P_2) pairs. Consequently, the overall geometrical arrangement relies on two distinct octahedral units, FeS_6 and P_2S_6 . Further structural details can be easily understood by considering the doubled formula unit, i.e., $\text{Fe}_2\text{P}_2\text{S}_6$ with one P_2 pair. Each S atom is bonded with one P and two Fe^{2+} centers [29]. The P_2 pair possesses a formal valency of +8 (P_2^{+8}), where each P contributes 3s² and 3p² electrons in the valence-band states and one remaining electron for P-P bond formation. In addition to this, each S and Fe contributes 3s², 3p⁴, and 4s² outer-shell electrons, respectively. Therefore, in a $\text{Fe}_2\text{P}_2\text{S}_6$ unit, a total of 48 electrons fill up the valence-band states, and the Fe^{2+} metal cores are stabilized by the $[\text{PS}_3]^{-2}$ units [29].

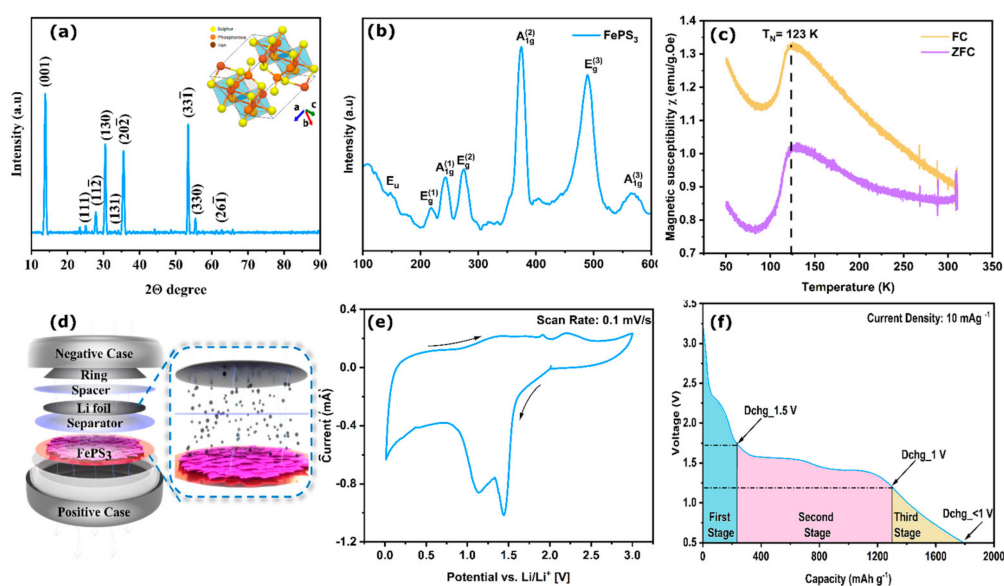


Figure 2. (a) X-ray diffraction pattern, (inset: geometric model of FePS_3 molecule with octahedral voids), (b) Raman characterization, and (c) vibrating sample magnetometer (VSM) analysis of as-synthesized FePS_3 . χ vs. T plot for pristine FePS_3 in the temperature range of 50–300 K under an applied magnetic field of $H = 100$ Oe. FC and ZFC represent field cooling and zero field cooling, represented by blue and green solid lines. (d) Schematic representation of lithium primary battery with FePS_3 nanoflakes as cathode. (e) CV plots at 0.1 mV s^{-1} . (f) Galvanostatic full-discharge profile of FePS_3 cathode with proposed three-stage mechanism.

2.3. Cathode Properties of FePS_3 Material

The electrochemical discharge performances of the FePS_3 system as a cathode material in an LPB is checked using a Li ion half cell, the details of which are given in the experimental details section. The electrochemical performance of the as-synthesized FePS_3 coated on copper foil was investigated using CR2016 coin cells. CR2016 coin cells were assembled using the conventional method. Coin cell testing specifications used in sample preparation for the characterizations are given in Table S1, ESI Section S7. The cell showed an open-circuit voltage (OCV) of 3.2 V when assembled and was galvanostatically (10 mA g^{-1}) discharged until 0.5 V vs. Li/Li^+ (foil) as the anode. Figure 2d shows the schematic representation of a lithium primary coin-cell assembly with FePS_3 nanoflakes as the cathode material. The cyclic voltametric (CV) test was performed at a scan rate of 0.1 mV s^{-1} to analyze the electrochemical redox reactions involved. The two reduction peaks (Figure 2e) can be found near 1.4 and 1.1 V, indicating the two stages of lithiation in FePS_3 . Similarly, during the anodic sweep, the oxidation peaks located at 1.9 and 2.2 V vs. Li/Li^+ can be correlated to the corresponding de-lithiation steps. The cathodic current in the region from 0.9 V to 0.5 V could be ascribed to the irreversible reaction between the active materials and the electrolyte towards the formation of the CEI (cathode electrolyte interface), which is discussed later. To confirm the lithium storage mechanism in the FePS_3 electrode, a freshly assembled cell was galvanostatically discharged at a current density of 10 mA g^{-1} , as shown in Figure 2f. The voltage plateaus located at around 1.6 V and 1.25 V in the discharge profile are in accordance with the CV data. The discharge capacity with respect to the total mass loading of the active material FePS_3 is found to be 1791 mAh g^{-1} , which is about 3.5 times that of fluorographene (520 mAh g^{-1}), which is one of the more common primary battery systems. Additionally, the galvanostatic discharge performance and CV data of FePS_3 as a secondary battery are shown in Figure S8a,b.

2.4. Post-mortem Analyses of FePS₃ Material

We emphasize that the obtained discharge capacity of 1791 mA h g⁻¹ is significantly greater than that of the theoretical value for FePS₃ (1318 mA h g⁻¹) [22]. From the discharge plateau (Figure 2f), it is suspected that the total capacity contribution could be due to three distinct reactions that occur in the three different stages. The first stage could be due to the presence of unreacted defect moieties present in the sample. The second stage, which is the main contributor to the capacity, could be the active material FePS₃, and the sloping voltage plateaus that occur below 1 V could be the third stage, which is the formation of a stable CEI film on the surface of the electrode (in accordance with the CV plot).

In order to verify our proposition, the post-mortem analysis of the battery cells discharged at different stages was conducted using XPS- and SEM-based analyses. The chemical state information of the pristine and discharged electrodes, acquired through XPS, give significant understanding of the mechanism. The detailed mechanism of all the three stages is discussed below. As shown in Figure 3, the XPS investigation of the ante- and post-discharged cells at the photoemission lines of S 2p, P 2p, and Fe 2p (Figure S6.3 ESI) were recorded. From now on, the uncycled electrode prior to discharge is named as pristine FePS₃, and the cells discharged until 1.5 V, 1 V, and 0.5 V are named as DChg_1.5 V, DChg_1 V, and DChg_<1 V.

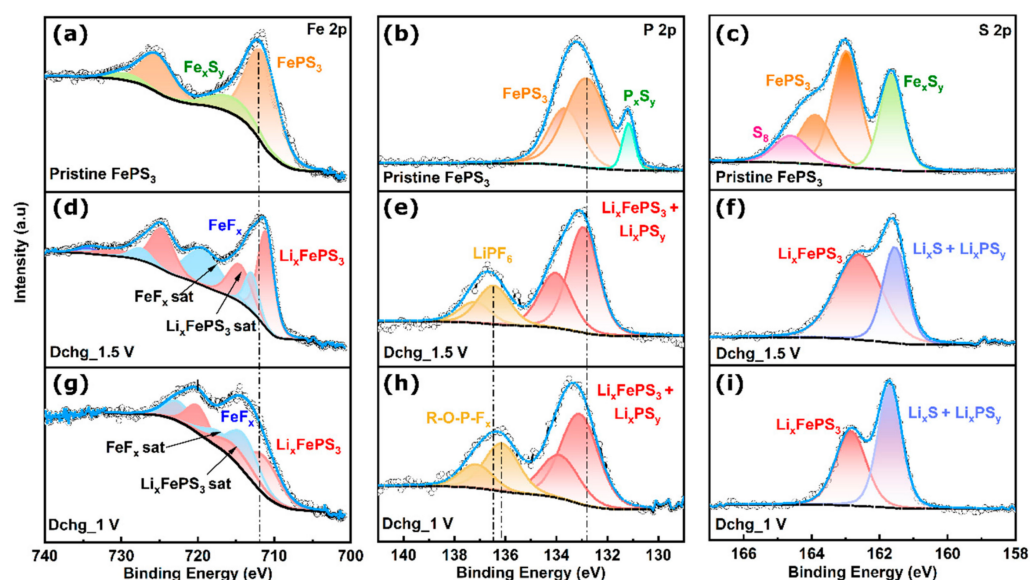
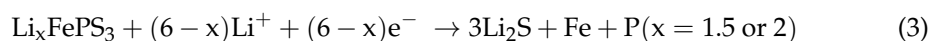
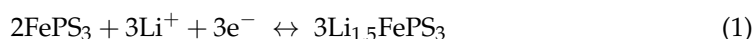


Figure 3. Comparison of high-resolution XPS spectra of pristine FePS₃ and discharged FePS₃ lithium primary battery during different stages of discharge. (a,d,g) High-resolution XPS spectra of Fe 2p; (b,e,h) high-resolution XPS spectra of P 2p; and (c,f,i) high-resolution XPS spectra of S 2p of pristine FePS₃ and discharged FePS₃ until 1.5 and 1 V.

From Figure 2f, it can be identified that the second stage is the main contributor towards the capacity, i.e., due to the main component FePS₃. The electrochemical discharge reaction mechanisms of Li ion insertion in FePS₃ were studied earlier and can be described as in Equations (1)–(3):



Initially, at $x = 1.5$, topochemical storage mechanism through geometric factors, i.e., filling of octahedral voids, would contribute up to 219 mA h g⁻¹ to the capacity (Equation (1)). Thereafter, the formation of Li_{1.5} FePS₃, and the further addition of Li ions can proceed

through Equations (2) and (3) simultaneously. For $x = 2$, the d-levels of Fe^{2+} cations act as acceptor centers, where Li ion intercalation is accompanied by a reduction of cations (Fe^{2+} to Fe^0) in the MPX_3 structure. This conversion shows a discharge capacity of 292 mAh g^{-1} following Equation (2). Nevertheless, the higher discharge capacity of 1318 mAh g^{-1} is achieved due to the irreversible changes that occur in the active cathodic material, resulting in Li_2S as the final discharge product, as shown in Equation (3). To confirm that the above intercalation is followed by a conversion mechanism, all the discharged electrodes (DChg_1.5 V, DChg_1 V, and DChg_<1 V) were investigated through XPS.

The high-resolution Fe 2p XPS spectrum of Dchg_1.5 V sample shows two spin-orbit-coupled peaks at 711.1 eV (Fe 2p_{3/2}) and 724.8 eV (Fe 2p_{1/2}) (Figure 3d). It can be noted that the Fe 2p_{3/2} binding energy (BE) peak is downshifted by 0.9 eV compared to the pristine FePS_3 peak at 712.0 eV (Figure 3a), indicating the formation of Li_xFePS_3 ($x \leq 1.5$), accompanied by the reduction of Fe^{2+} in accordance to Equation (1). The further downshift of Fe 2p_{3/2} binding energy for the sample Dchg_1 V (Figure 3g) indicates an increase in the Li content ($x > 1.5$) in Li_xFePS_3 as in Equation (2), possibly by $2e^-$ reduction of Fe^{2+} to Fe^0 . Moreover, the decrease in the peak intensity of Fe 2p_{3/2} for Dchg_1 V indicates the increase in the irreversible reactions as in Equation (3). Similarly, the comparison of the high-resolution P 2p (2p_{3/2} and 2p_{1/2}) XPS spectrum of the pristine FePS_3 , Dchg_1.5 V, and Dchg_1 V samples also supports the above-mentioned hypothesis. The slight consecutive upshifts in the binding energy of 2p_{3/2} from pristine FePS_3 (132.9 eV) to Dchg_1.5 V (133 eV) and further to Dchg_1 V (133.1 eV) are visible in Figure 3b,e,h. These indicate the replacement of Fe centers by more electropositive Li in -P-S-Fe- bonds during Li-ion insertion at the Fe^{2+} centers, followed by their reduction and formation of Li_xFePS_3 ($x \geq 1.5$). The high-resolution S 2p XPS spectra for all three samples do not show any appreciable change for the binding energy peak at around 162.9 eV. However, it is taken into consideration for determining the structural dissociation mentioned in Equation (3). The enhancement in the intensity of the binding energy peak at around 161.6 eV corresponding to Li_2S relative to that of the Li_xFePS_3 from Dchg_1.5 V to Dchg_1 V confirms the overall collapse of the Li_xFePS_3 structure upon further addition of Li ions and formation of Li_2S as the final discharge product.

The lithium intercalation and conversion mechanism discussed above during the discharge in FePS_3 are further supported by high-resolution Li 1s spectra. The Dchg_1.5 V sample shows the presence of both Li_xFePS_3 and Li_2S , as the Li 1s binding energy peaks for both are overlapping at 55.6 eV. However, as the discharge depth increases in Dchg_1 V, a slight downshift of 0.2 eV is observed in the binding energy peak that can be ascribed to the increase in Li_2S concentration, as shown in Equation (3).

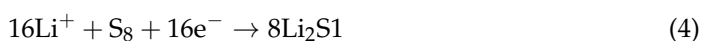
Hence, the main lithium storage mechanism for FePS_3 (second stage) is confirmed to proceed by the formation of the Li_xFePS_3 initially ($x \geq 1.5$), followed by the formation of Li_2S on the subsequent addition of Li ions (Equation (3)), which gives rise to a discharge capacity of 1318 mAh g^{-1} . However, the observed discharge capacity of 1791 mAh g^{-1} can be explained as the contribution of two different stages (Figure 2f): the first stage and third stage (discussed later). Before that, a question that may arise is whether the Fe or P that are formed in accordance to Equation (3) act as extra storage sites for lithium. We can clearly omit this possibility, as no peak corresponding to either Li_3P or any lithium-iron compound formation is observed in the high-resolution Li 1s, P 2p, and Fe 2p XPS spectra. Instead, the spectra show the presence of Fe-F and P-F bond formation with the increase in the depth of discharge, as shown in Figure 3d–h. This can be attributed to the iron-catalyzed dissociation of the electrolyte, which is LiPF_6 , at a longer discharge period. Such dissociations are also reported for different transition metals [30,31]. For instance, J Park et al. [32] reported that Fe-based electrodes promote severe electrolyte decomposition (especially PF_6 -based electrolyte) and subsequent growth of a thick interface layer. In this case also, on dissociation of LiPF_6 , the P-F bond formation happens prior to any lithium intercalation in P (discussed in detail in the later part).

3. Discussion

3.1. Reasons for the Additional Capacity

The observed extra storage capacity in comparison to the theoretical limit is due to the contribution from the other two stages, as discussed here.

As explained in the beginning (first stage), the formation of FePS₃ happens via the formation of the FeS_x and PS_y units. However, some of the unreacted sulfur (S₈) along with defect moieties generated during the synthesis, such as FeS_x and P_xS_y, contribute to the extra capacity. Their presence along with the pristine sample is confirmed by the high-resolution XPS spectra of pristine FePS₃. In high-resolution S 2p spectra, the peaks at binding energy 164.4 eV and 161.6 eV correspond to the presence of sulfur (S₈) and FeS_x, respectively, while the S 2p binding energy peaks for P-S-P moieties are supposed to overlap with FePS₃ at around 162.9 eV. Additionally, the high-resolution Fe 2p signals at binding energy 716.30 eV (Fe 2p 3/2) and 729.6 eV (Fe 2p 1/2) correspond to the presence of FeS_x. On the other hand, the sharp peak at 131.2 eV in P 2p high-resolution spectra indicates the presence of P-S-P moieties. Therefore, the first stage depicts the lithium storage in these three moieties according to the following equations:



The high-resolution XPS spectra of the discharged electrodes, discussed before, was further analyzed to confirm the discharge reactions mentioned in the Equations (4)–(6) during the first stage. Unlike the second stage, where Li₂S was the final discharge product after the FePS₃ dissociation, Li₂S is formed as the result of unreacted S and FeS_x moieties present in the sample in the first stage. The total contribution of such defect moieties towards the capacity is particularly smaller (<250 mAh g⁻¹). It is important to note that the sulfur-based cathodes are limited by the low practically achievable energy density. For instance, in 2015, Y. Ma [33] and colleagues reported a Li-S battery that could achieve an energy density of hardly 504 Wh Kg⁻¹ even though the theoretical energy density was 2600 Wh Kg⁻¹.

As discussed in the second stage, the high-resolution XPS spectra of S 2p and Li 1s (ESI) for Dchg_1.5 V shows the presence of both Li_xFePS₃ and Li₂S. The Li₂S present here is attributed to the discharged product formed in the first stage due to the three other moieties present in the system (Equations (4) and (5)), while the increase in the Li₂S content in Dchg_1 V is due to the disintegration of the Li_xFePS₃ with the further addition of Li ions. The other contributor towards the additional capacity is the P_xS_y moiety, according to Equation (6). The binding energy for Li_xPS_y in high-resolution P 2p and S 2p XPS spectra overlays with that of the other discharge products, Li_xFePS₃ and Li₂S, respectively (Figure 3e,f,h,i). As discussed above, the second stage corresponds to the interaction of lithium in to FePS₃.

In the third stage, the extra capacity can be assigned to the Li ions reacting with the decomposed products of the electrolyte and resulting in the formation of a CEI. At high depths of discharge, the samples Dchg_1 V and Dchg_<1 V show the emergence of LiF along with the main discharge products. The presence of the peak at binding energy of 56.2 eV in the high-resolution Li 1s spectra of Dchg_1 V and Dchg_<1 V clearly shows the dominance of the LiF phase (Figure S6.3 ESI). As mentioned earlier, in the second stage, the Fe-based electrodes or metallic iron formed during the discharge step of Equation (3) can catalyze the PF₆-based electrolyte decomposition, as shown in Equation (7), followed by the LiF formation in Equation (8):



LiF is the main component of the CEI and contributes towards the extra capacity. Such electrolyte (salt) decomposition resulting in the formation of LiF is in accordance with the previous reports where the CEI only contains salt-based products such as LiF, Li_xF_y , and $\text{Li}_x\text{PO}_y\text{F}_z$ [34]. LiF has a high theoretical specific capacity of around 1000 mAh g^{-1} and hence contributes to the extra capacity towards the end. Even though the system discussed here is a primary battery, the study of the CEI formation can be extended to the secondary systems as well. A stable CEI is imperative in order to increase the thermal stability of the aggressive cathodes, evade the inter-face side reactions, and guarantee the electrochemical performance. CEI with high inorganic content (for example, Li_2CO_3 and LiF) would function as an electronic insulator and facilitate the desired Li^+ transport. A well-regulated growth of robust cathode–electrolyte interphase (CEI) with high inorganic content is the most beneficial approach to tackle the thermal runaway concerns [35].

The above-mentioned three-stage mechanism is further supported by SEM (Figure 4a–d). The consistent increase in the cross-sectional thickness from the pristine FePS_3 to Dchg_1.5 V and finally to Dchg_1 V electrode confirms the lithium intercalation over the increased discharge depth (supporting information, Figure S9 ESI). The elemental mapping is also performed by EDS of the fully discharged sample. The Figure 4a–d show the presence of sulfur (S) (atomic percentage = 5%) until a certain thickness, indicating the presence of Li_2S as in Equation (3) during the initial stage of discharge. The percentage of other elements starts increasing while moving towards the top, i.e., Fe (atomic percentage = 2.4%) and F (atomic percentage = 25%), indicating the formation of fluorine-based decomposition products (discussed later). The high percentage of fluorine relative to other elements present indicates the presence of LiF as the main product towards the end of the discharge (Equation (8)), in tune with the XPS measurements. Hence, the main contributor towards the total capacity is the FePS_3 (discussed in second stage), while the defect moieties and CEI formation result in the extra capacity, as discussed in first and third stage, respectively. We expect that such controlled formation of CEI layer via LiF formation would open up innovative ways of engineering CEI formation strategies, as it is crucial for the performance of various secondary batteries as well [36].

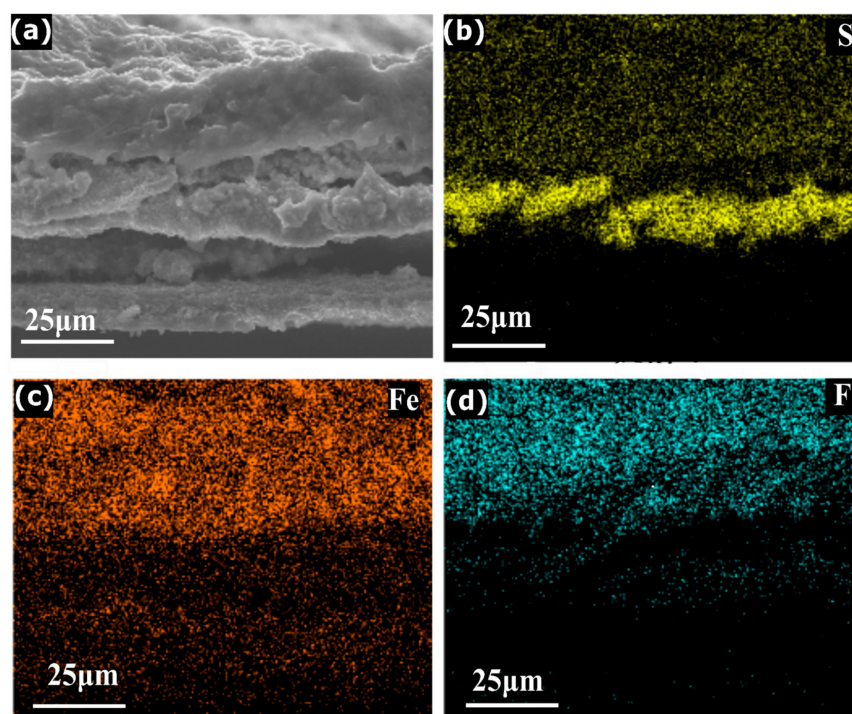


Figure 4. SEM and EDS mapping analysis of a cross-section of the FePS_3 electrode discharged till 0.5 V: (a) secondary electron image of SEM and (b) S (yellow), (c) Fe (orange) and (d) F (blue) elemental mapping using EDS.

3.2. Electrolyte Decomposition

In general, primary batteries are known to run for longer periods. Hence, both during the discharge and after the complete utilization of a battery, the study of the degradation products is important in two aspects. Firstly, treatment of the used components of the battery becomes easier with prior knowledge of the species present in the system [37–39]. Secondly, in biological systems where the batteries are used for longer runs, the formation of the hazardous chemicals is undesirable [40,41]. In this study, the main changes (electrolyte decomposition) are also observed at lower discharge voltages. These are the reactions that caused the further formation of CEI products in the $D_{chg} < 1$ V electrodes, confirmed by high-resolution Fe 2p, P 2p, S 2p, (Figure S6.2, ESI), C 1s (Figure S6.4, ESI), and Li 1s XPS spectra.



The uniform distribution of phosphorus, oxygen, and carbon on the surface of the discharged electrodes also supports the electrolyte decomposition pathways, as shown in Equations (9)–(12) and given in electronic Supplementary Information (Figure S10).

3.3. Three-Stage Discharge Mechanism in FePS₃ Systems

Based on the findings acquired through XPS and SEM analyses, we propose a three-stage discharge mechanism for the FePS₃ system, validating the obtained very high capacity (1791 mAh g^{−1}) (Figure 2f). During the first stage, defect species that developed on account of unreacted S, FeS_x, and P_xS_y are recognized in the sample that contribute towards the initial capacity. However, the overall capacity contribution from such defect moieties is explicitly less than 250 mAh g^{−1}. The main discharge product during this stage is Li₂S due to the lithiation in defect moieties (first stage, shaded in blue color). In the second stage, the FePS₃ itself is the principal capacity storage contributor. Meanwhile, the discharge proceeds via lithium intercalation and conversion mechanism within FePS₃ to form Li_xFePS₃ ($x \leq 2$) along with the formation of dissociation products including Li₂S, P, and metallic Fe (second stage, shaded in pink color). At this stage, the initial formation of CEI is also recognized. The third stage includes the decomposition of the electrolyte that captures the Li ions, causing a stable CEI formation (particularly LiF) and contributing towards the excess capacity (third stage, shaded in yellow color). Moreover, several irreversible reactions are also occurring due to electrode/electrolyte decomposition, as shown above.

3.4. Performance of FePS₃ in LPB

The primary cells should function at high discharge loads as well as work for a vast range of applications. Hence, we studied the rate capability at different current densities for the FePS₃-assisted Li ion cells. The cells were discharged at the current densities of 10, 50, 100, 250, 500, and 1000 mA g^{−1}. The plots are shown in Figure 5a. It was observed that even at the higher current densities of 500–1000 mA g^{−1}, the cells show high discharge capacities around 1000 and 900 mAh g^{−1} (Figure 5b). This shows the high efficiency of LiFePS₃ as a primary storage material even for high loads. Further, a full cell experiment using lithium as cathode instead of lithiated graphite delivered a high capacity of 1131 mAh g^{−1}, presenting its exceptional behavior as a primary battery. More details of the full cell experiment are given in Section S11 ESI. A comparison plot of FePS₃ battery performance with other reported materials is shown in Figure 5c and Table S2, ESI. The high capacity and high energy density of the FePS₃ showcase the best value among previous reports. Additionally, a table is tabulated (Table S2, Section S12, ESI) to give a compact view of the reported primary batteries with specific capacity, energy density, current density, and voltage window. Finally, a small motor (1.2 V/15 mA) was operated (video of the working

motor is shown in the supporting information, Video S1) using the assembled battery for demonstration purposes (Figure 5c inset) to indicate the high capacity of the FePS₃-based primary cells. The configuration for the demonstration was adapted from a previous study [42]. The movie Video S1 displays the motor running for around 45 s using a single coin cell. The Figure 5c inset shows the on and off state of the motor. Furthermore, the shelf life of the battery was calculated using an aged cell kept for one month after assembling. The aged cell exhibited specific capacity of 1771 mAh g⁻¹ after one month, which is almost nearer to a freshly assembled cell (Figure 5d). The overlapping, overlaid data of fresh and aged cells show no evidence of any cathodic corrosion, electrolyte degradation, or side reactions, highlighting the superiority of FePS₃ as a lithium primary battery without any self-discharge. The cost analysis of a single coin cell was estimated using the details given in Table S3, ESI Section S13. The estimated cost is USD 0.17, in which USD 0.15 is the cost of assembling parts. The given cost analysis indicates the possibilities of low-cost battery development using FePS₃ as the cathode material.

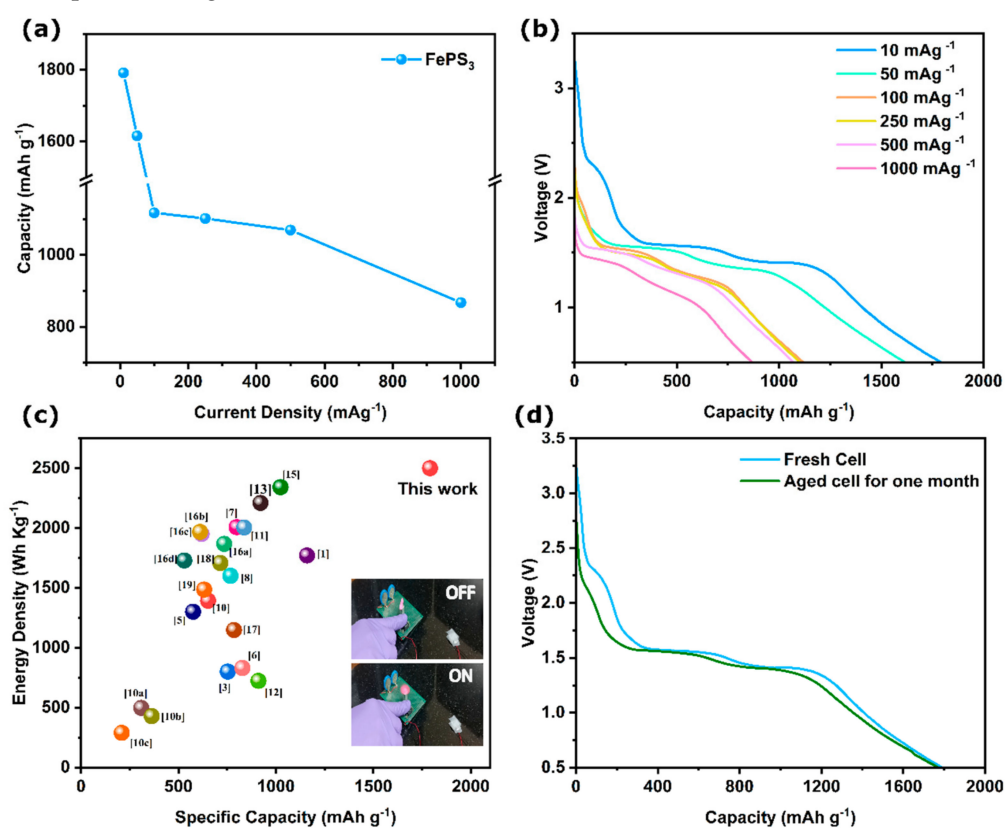


Figure 5. (a) Galvanostatic full-discharge profiles and (b) rate capability of FePS₃ primary battery at various current densities. (c) Comparison analysis graph of reported batteries with this work with the photographic images of FePS₃-based primary cell (battery) running a small motor (1.2 V/15 mA) as inset. (d) Shelf-life study of the battery tested one month after assembling, where the cells are discharged at 10 mA g⁻¹.

4. Materials and Methods

4.1. Experimental Section

Materials: Iron (III) chloride hexahydrate (FeCl₃·6H₂O), sulfur powder, and lithium hexafluorophosphate (LiPF₆) in DMC solvent were purchased from Sigma Aldrich Inc. St. Louis, MO, USA. Phosphorus red was purchased from Sisco Research Laboratories Pvt Ltd, Mumbai, India. Sodium chloride (NaCl) extra pure was purchased from S.D fine Chem Limited (Chennai, India). 1-Methyl-2 pyrrolidinone (NMP) was purchased from Avra Synthesis Pvt Ltd, Hyderabad, India.

4.2. Preparation of FePS₃ Electrode

The electrode preparation was performed in the traditional way by grinding 80% of FePS₃ material, 10% carbon black, and 10% (polyvinylidene fluoride) PVDF into a semi-thick slurry using NMP. The slurry was coated on battery-grade copper foil using a doctor blade. The electrode was dried at 80 °C for 8 h. Circular discs (diameter = 1 cm) were cut off from the same and used to assemble the CR2016-coin cell battery with lithium foil as the counter electrode. The typical mass load of active material was controlled to be about 1 to 2 mg cm⁻².

4.3. Characterization Techniques

To determine the vibrational Raman modes of FePS₃, Renishaw inVia Raman microscope (532 nm excitation) was used. Further, to know the surface topography and composition of the sample, a field emission scanning electron microscope (FESEM) JEOL JSM-7200F (JEOL Ltd, Tokyo, Japan) along with EDS was used. A transmission electron microscope TEM, JEM-2100F (JEOL Ltd, Tokyo, Japan) with acceleration voltage of 300 kV (aberration corrected) was used for TEM analysis of the samples. The crystallinity of the materials was studied using X-ray diffraction (Bruker Tensor-27). X-ray photoelectron spectroscopy (XPS) results from Thermo Fisher Scientific (Cleveland, OH, USA) ESCALAB Xi⁺ provided the surface elemental composition and electronic states of the samples. Thermogravimetric analyses (TGA) were operated with a TA Instruments (TGA 550, TA instruments, New Castle DE, USA) apparatus at a heating rate of 10 °C min⁻¹ under nitrogen flow.

4.4. Electrochemical Measurements

A Biologic SP-300 potentiostat (Biologic, Vaucanson, France) was used for the electrochemical measurements (CV). The cyclic voltametric tests were carried out using an adapter with a two-electrode cell, which was assembled using the FePS₃ electrode as the working electrode and lithium metal as both the counter and reference electrodes. The CV was performed with a 0.1 mV/s scan rate. Further, the battery cell assembly was carried out in an Ar-filled glovebox with <0.1 ppm H₂O content. Moreover, galvanostatic charge and discharge tests were conducted using a Neware battery-testing system in the voltage range of 0.01 to 3.0 V vs. Li/Li⁺.

5. Conclusions

A layered metal phosphide trichalcogenide-based, i.e., FePS₃-based, economically viable, environmentally benign, high-capacity cathode material for LPB is demonstrated herein. The salt-template-assisted synthesis method provided here put forward a scalable but simple and efficient synthesis route for FePS₃ nanoflakes. Moreover, the Li ion cells constructed showed a very high rate capability (1 A g⁻¹) and specific capacity (867 mAh g⁻¹) compared to that of the previously reported primary battery electrode materials. A detailed post-mortem analysis unraveled the discharge mechanism in FePS₃, leading to its high capacity. A three-staged discharge mechanism is proposed in accordance with the obtained results. The LPB assembled with FePS₃ show a high discharge capacity of 1791 mAh g⁻¹ and a high energy density of 2500 Wh Kg⁻¹, with a long shelf life. The FePS₃ LPB delivered a maximum specific capacity of 867 mAh g⁻¹ even at a high current density of 1 A g⁻¹, which is higher than all the previously reported systems. This work provides a simple and low-cost approach to develop MPX₃-based, highly efficient primary battery systems, underling its capability towards a vast range of practical applications.

Supplementary Materials: Electronic Supplementary Information (ESI) can be downloaded at: <https://www.mdpi.com/article/10.3390/molecules28020537/s1> or from the author. The ESI contains details of materials characterization and electrochemical data along with a video of the functioning of a motor [43–56].

Author Contributions: Conceptualization, S.L., S.S.S., and T.N.N.; methodology, S.L.; software, S.L.; validation, S.L.; formal analysis, S.L., P.T., and S.S.S.; investigation, S.L.; resources, T.N.N.; data curation, S.L. and P.T.; writing—original draft preparation, S.L.; writing—review and editing, P.T., S.S.S., T.N.N., and Z.D.; visualization, S.L., P.T., S.S.S., and T.N.N.; supervision, T.N.N. and Z.D.; project administration, T.N.N.; funding acquisition, T.N.N. All authors have read and agreed to the published version of the manuscript.

Funding: This research was funded Department of Atomic Energy, Government of India, under Project Identification No. RTI 4007, Postdoctoral Fund of Shaanxi Province (2017BSHEDZZ122) and the Fundamental Scientific Research Project of Xi'an Jiaotong University (xzy022022025).

Institutional Review Board Statement: Not applicable.

Informed Consent Statement: Not applicable.

Data Availability Statement: Not applicable.

Acknowledgments: S.L. thanks TIFR Hyderabad and Xi'an Jiaotong University, School of Material Science and Engineering Facilities, for the support. Thanks to Swapna S Nair (Kerala University, India) for helping with VSM analysis. Authors from TIFR acknowledge the support of the Department of Atomic Energy, Government of India, under Project Identification No. RTI 4007. Figures 1a and 2d were designed by S.L. and drawn by Ashique Lal.

Conflicts of Interest: The authors declare no conflict of interest.

Sample Availability: Samples of the compounds are available from the authors.

References

1. Cao, W.; Zhang, J.; Li, H. Batteries with high theoretical energy densities. *Energy Storage Mater.* **2020**, *26*, 46–55. [[CrossRef](#)]
2. Liu, Y.; Su, M.Y.; Gu, Z.Y.; Zhang, K.Y.; Wang, X.T.; Du, M.; Guo, J.Z.; Wu, X.L. Advanced Lithium Primary Batteries: Key Materials, Research Progresses and Challenges. *Chem. Rec.* **2022**, *22*, e202200081. [[CrossRef](#)] [[PubMed](#)]
3. Sun, P.; Bai, P.; Chen, Z.; Su, H.; Yang, J.; Xu, K.; Xu, Y. A Lithium–Organic Primary Battery. *Small* **2020**, *16*, 1906462. [[CrossRef](#)] [[PubMed](#)]
4. Zhou, X.; Li, P.; Tang, Z.; Liu, J.; Zhang, S.; Zhou, Y.; Tian, X. FEC Additive for Improved SEI Film and Electrochemical Performance of the Lithium Primary Battery. *Energies* **2021**, *14*, 7467. [[CrossRef](#)]
5. Li, L.; Zhu, L.; Pan, Y.; Lei, W.; Ma, Z.; Li, Z.; Cheng, J.; Zhou, J. Integrated polyaniline-coated CF_x cathode materials with enhanced electrochemical capabilities for Li/CF_x primary battery. *Int. J. Electrochem. Sci.* **2016**, *11*, 6838–6847. [[CrossRef](#)]
6. Damien, D.; Sudeep, P.; Narayanan, T.; Anantharaman, M.; Ajayan, P.; Shaijumon, M. Fluorinated graphene based electrodes for high performance primary lithium batteries. *RSC Adv.* **2013**, *3*, 25702–25706. [[CrossRef](#)]
7. Wanigarathna, D.J.; Gao, J.; Takanami, T.; Zhang, Q.; Liu, B. Adsorption separation of R-22, R-32 and R-125 fluorocarbons using 4A molecular sieve zeolite. *Chem. Sel.* **2016**, *1*, 3718–3722. [[CrossRef](#)]
8. Yang, X.-X.; Zhang, G.-J.; Bai, B.-S.; Li, Y.; Li, Y.-X.; Yang, Y.; Jian, X.; Wang, X.-W. Fluorinated graphite nanosheets for ultrahigh-capacity lithium primary batteries. *Rare Met.* **2021**, *40*, 1708–1718. [[CrossRef](#)]
9. Sun, L.; Peng, C.; Kong, L.; Li, Y.; Feng, W. Interface-Structure-Modulated CuF₂/CF_x Composites for High-Performance Lithium Primary Batteries. *Energy Environ. Mater.* **2022**. [[CrossRef](#)]
10. Li, Y.; Wu, X.; Liu, C.; Wang, S.; Zhou, P.; Zhou, T.; Miao, Z.; Xing, W.; Zhuo, S.; Zhou, J. Fluorinated multi-walled carbon nanotubes as cathode materials of lithium and sodium primary batteries: Effect of graphitization of carbon nanotubes. *J. Mater. Chem.* **2019**, *7*, 7128–7137. [[CrossRef](#)]
11. Lisbona, D.; Snee, T. A review of hazards associated with primary lithium and lithium-ion batteries. *Process Saf. Environ. Prot.* **2011**, *89*, 434–442. [[CrossRef](#)]
12. Ma, H.; Zhang, S.; Ji, W.; Tao, Z.; Chen, J. α -CuV₂O₆ nanowires: Hydrothermal synthesis and primary lithium battery application. *J. Am. Chem. Soc.* **2008**, *130*, 5361–5367. [[CrossRef](#)] [[PubMed](#)]
13. Chen, K.; Merritt, D.R.; Howard, W.G.; Schmidt, C.L.; Skarstad, P.M. Hybrid cathode lithium batteries for implantable medical applications. *J. Power Sources* **2006**, *162*, 837–840. [[CrossRef](#)]
14. Chang, Y.; Wang, M.; Wang, S.; Na, J.; Bund, A.; Nanjundan, A.K.; Yamauchi, Y. Ultralong storage life of Li/MnO₂ primary batteries using MnO₂-(CF_x)_n with C–F semi-ionic bond as cathode materials. *Electrochim. Acta* **2019**, *320*, 134618. [[CrossRef](#)]
15. Tian, Y.; Chen, Y.; Liu, Y.; Li, H.; Dai, Z. Elemental two-dimensional materials for Li/Na-ion battery anode applications. *Chem. Rec.* **2022**, *22*, e202200123. [[CrossRef](#)]
16. Nithya, C.; Gopukumar, S. Nanostructured transition metal chalcogenides for rechargeable batteries. In *Nanobatteries and Nanogenerators*; Elsevier: Amsterdam, The Netherlands, 2021; pp. 383–431.
17. Wang, F.; Shifa, T.A.; Yu, P.; He, P.; Liu, Y.; Wang, F.; Wang, Z.; Zhan, X.; Lou, X.; Xia, F. New frontiers on van der Waals layered metal phosphorous trichalcogenides. *Adv. Funct. Mater.* **2018**, *28*, 1802151. [[CrossRef](#)]

18. Liu, Y.; Chen, Y.; Tian, Y.; Sakthivel, T.; Liu, H.; Guo, S.; Zeng, H.; Dai, Z. Synergizing Hydrogen spillover and deprotonation by internal polarization field in a MoS₂/NiPS₃ vertical heterostructure for boosted water electrolysis. *Adv. Mater.* **2022**, *34*, 2203615. [[CrossRef](#)]
19. Jana, R.; Chowdhury, C.; Datta, A. Transition-Metal Phosphorus Trisulfides and its Vacancy Defects: Emergence of a New Class of Anode Material for Li-Ion Batteries. *ChemSusChem* **2020**, *13*, 3855–3864. [[CrossRef](#)]
20. Kuzminskii, Y.V.; Voronin, B.; Redin, N. Iron and nickel phosphorus trisulfides as electroactive materials for primary lithium batteries. *J. Power Sources* **1995**, *55*, 133–141. [[CrossRef](#)]
21. Liu, C.; Neale, Z.G.; Cao, G. Understanding electrochemical potentials of cathode materials in rechargeable batteries. *Mater. Today* **2016**, *19*, 109–123. [[CrossRef](#)]
22. Fujii, Y.; Miura, A.; Rosero-Navarro, N.C.; Higuchi, M.; Tadanaga, K. FePS₃ electrodes in all-solid-state lithium secondary batteries using sulfide-based solid electrolytes. *Electrochim. Acta* **2017**, *241*, 370–374. [[CrossRef](#)]
23. Gusmão, R.; Sofer, Z.; Pumera, M. Metal phosphorous trichalcogenides (MPCh₃): From synthesis to contemporary energy challenges. *Angew. Chem. Int. Ed. Engl.* **2019**, *58*, 9326–9337. [[CrossRef](#)] [[PubMed](#)]
24. Huang, H.; Li, F.; Xue, Q.; Zhang, Y.; Yin, S.; Chen, Y. Salt-Templated Construction of Ultrathin Cobalt Doped Iron Thiophosphite Nanosheets toward Electrochemical Ammonia Synthesis. *Small* **2019**, *15*, 1903500. [[CrossRef](#)] [[PubMed](#)]
25. Kargar, F.; Coleman, E.A.; Ghosh, S.; Lee, J.; Gomez, M.J.; Liu, Y.; Magana, A.S.; Barani, Z.; Mohammadzadeh, A.; Debnath, B. Phonon and thermal properties of quasi-two-dimensional FePS₃ and MnPS₃ antiferromagnetic semiconductors. *ACS Nano* **2020**, *14*, 2424–2435. [[CrossRef](#)] [[PubMed](#)]
26. Lee, J.-U.; Lee, S.; Ryoo, J.H.; Kang, S.; Kim, T.Y.; Kim, P.; Park, C.-H.; Park, J.-G.; Cheong, H. Ising-type magnetic ordering in atomically thin FePS₃. *Nano Lett.* **2016**, *16*, 7433–7438. [[CrossRef](#)] [[PubMed](#)]
27. Glass, D.E.; Jones, J.P.; Shevade, A.V.; Bugga, R.V. Transition Metal Phosphorous Trisulfides as Cathode Materials in High Temperatures Batteries. *J. Electrochem. Soc.* **2020**, *167*, 110512. [[CrossRef](#)]
28. Fan, C.-Y.; Zhang, X.-H.; Shi, Y.-H.; Xu, H.-Y.; Zhang, J.-P.; Wu, X.-L. 2D few-layer iron phosphosulfide: A self-buffer heterophase structure induced by irreversible breakage of p–s bonds for high-performance lithium/sodium storage. *J. Mater. Chem.* **2019**, *7*, 1529–1538. [[CrossRef](#)]
29. Khumalo, F.; Hughes, H. Reflectance spectra of some FePS₃-type layer compounds in the vacuum ultraviolet. *Phys. Rev. Lett. B* **1981**, *23*, 5375. [[CrossRef](#)]
30. Vilá, R.A.; Huang, W.; Cui, Y. Nickel impurities in the solid-electrolyte interphase of lithium-metal anodes revealed by cryogenic electron microscopy. *Cell Rep. Phys. Sci.* **2020**, *1*, 100188. [[CrossRef](#)]
31. Wang, C.; Xing, L.; Vatamanu, J.; Chen, Z.; Lan, G.; Li, W.; Xu, K. Overlooked electrolyte destabilization by manganese (II) in lithium-ion batteries. *Nat. Commun.* **2019**, *10*, 3423. [[CrossRef](#)]
32. Park, J.; Ku, K.; Son, S.-B.; Gim, J.; Kim, Y.; Lee, E.; Johnson, C. Effect of Electrolytes on the Cathode-Electrolyte Interfacial Stability of Fe-Based Layered Cathodes for Sodium-Ion Batteries. *J. Electrochem. Soc.* **2022**, *169*, 030536. [[CrossRef](#)]
33. Ma, Y.; Zhang, H.; Wu, B.; Wang, M.; Li, X.; Zhang, H. Lithium sulfur primary battery with super high energy density: Based on the cauliflower-like structured C/S cathode. *Sci. Rep.* **2015**, *5*, 14949. [[CrossRef](#)] [[PubMed](#)]
34. Bhandari, A.; Bhattacharya, J.; Pala, R.G.S. Adsorption preference of HF over ethylene carbonate leads to dominant presence of fluoride products in LiFePO₄ cathode–electrolyte interface in Li-ion batteries. *J. Phys. Chem. C.* **2020**, *124*, 9170–9177. [[CrossRef](#)]
35. Wang, E.; Niu, Y.; Yin, Y.-X.; Guo, Y.-G. Manipulating electrode/electrolyte interphases of sodium-ion batteries: Strategies and perspectives. *ACS Mater. Lett.* **2020**, *3*, 18–41. [[CrossRef](#)]
36. Huang, Q.; Turcheniuk, K.; Ren, X.; Magasinski, A.; Song, A.-Y.; Xiao, Y.; Kim, D.; Yushin, G. Cycle stability of conversion-type iron fluoride lithium battery cathode at elevated temperatures in polymer electrolyte composites. *Nat. Mater.* **2019**, *18*, 1343–1349. [[CrossRef](#)]
37. Wei, Z.; Cheng, J.; Wang, R.; Li, Y.; Ren, Y. From spent Zn–MnO₂ primary batteries to rechargeable Zn–MnO₂ batteries: A novel directly recycling route with high battery performance. *J. Environ. Manag.* **2021**, *298*, 113473. [[CrossRef](#)]
38. Freitas, M.; Pegoretti, V.; Pietre, M. Recycling manganese from spent Zn–MnO₂ primary batteries. *J. Power Sources* **2007**, *164*, 947–952. [[CrossRef](#)]
39. Roy, J.J.; Rarotra, S.; Krikstolaityte, V.; Zhuoran, K.W.; Cindy, Y.D.I.; Tan, X.Y.; Carboni, M.; Meyer, D.; Yan, Q.; Srinivasan, M. Green recycling methods to treat lithium-ion batteries E-waste: A circular approach to sustainability. *Adv. Mater.* **2022**, *34*, 2103346. [[CrossRef](#)]
40. Moerke, C.; Wolff, A.; Ince, H.; Ortak, J.; Öner, A. New strategies for energy supply of cardiac implantable devices. *Herzschrittmacherther. Elektrophysiol.* **2022**, *33*, 224–231. [[CrossRef](#)]
41. Liang, S.; Zhou, J.; Pan, A.; Li, Y.; Chen, T.; Tian, Z.; Ding, H. Facile synthesis of β-AgVO₃ nanorods as cathode for primary lithium batteries. *Mater. Lett.* **2012**, *74*, 176–179. [[CrossRef](#)]
42. Thakur, P.; Puthirath, A.B.; Ajayan, P.M.; Narayanan, T.N. Iron carbide decorated carbon nanosphere-sheet hybrid based rechargeable high-capacity non-aqueous Li–O₂ batteries. *Carbon* **2022**, *196*, 320–326. [[CrossRef](#)]
43. Sun, C.; Feng, Y.; Li, Y.; Qin, C.; Zhang, Q.; Feng, W. Solvothermally exfoliated fluorographene for high-performance lithium primary batteries. *Nanoscale* **2014**, *6*, 2634–2641. [[CrossRef](#)] [[PubMed](#)]
44. Reddy, M.A.; Breitung, B.; Fichtner, M. Improving the energy density and power density of CF x by mechanical milling: A primary lithium battery electrode. *ACS Appl. Mater. Interfaces* **2013**, *5*, 11207–11211. [[CrossRef](#)] [[PubMed](#)]

45. Luo, Z.; Wang, X.; Chen, D.; Chang, Q.; Xie, S.; Ma, Z.; Lei, W.; Pan, J.; Pan, Y.; Huang, J. Ultrafast Li/fluorinated graphene primary batteries with high energy density and power density. *ACS Appl. Mater. Interfaces* **2021**, *13*, 18809–18820. [[CrossRef](#)] [[PubMed](#)]
46. Bonino, F.; Morzilli, S.; Scrosati, B. Electrochemical behaviour of metal sulphides as cathodes in primary lithium batteries. *J. Power Sources* **1985**, *14*, 65–69. [[CrossRef](#)]
47. Wang, L.; Li, Y.; Wang, S.; Zhou, P.; Zhao, Z.; Li, X.; Zhou, J.; Zhuo, S. Fluorinated nanographite as a cathode material for lithium primary batteries. *ChemElectroChem* **2019**, *6*, 2201–2207. [[CrossRef](#)]
48. Li, Q.; Xue, W.; Sun, X.; Yu, X.; Li, H.; Chen, L. Gaseous electrolyte additive BF₃ for high-power Li/CF_x primary batteries. *Energy Storage Mater.* **2021**, *38*, 482–488. [[CrossRef](#)]
49. Chen, Z.; Sun, P.; Bai, P.; Su, H.; Yang, J.; Liu, Y.; Xu, Y.; Geng, Y. A poorly soluble organic electrode material for high energy density lithium primary batteries based on a multi-electron reduction. *Chem. Comm.* **2021**, *57*, 10791–10794. [[CrossRef](#)]
50. Peng, S.; Yan, S.; Wang, N.; Nan, W.; Wang, J.; Chen, X.; Wang, C.; Qi, X.; Dai, S. Fluorinated graphene/sulfur hybrid cathode for high energy and high power density lithium primary batteries. *RSC Adv.* **2018**, *8*, 12701–12707. [[CrossRef](#)]
51. Hany, P.; Yazami, R.; Hamwi, A. Low-temperature carbon fluoride for high power density lithium primary batteries. *J. Power Sources* **1997**, *68*, 708–710. [[CrossRef](#)]
52. Yue, H.; Zhang, W.; Liu, H.; Liu, Z.; Zhong, G.; Yang, Y. Synthesis and characterization of fluorinated carbon nanotubes for lithium primary batteries with high power density. *Nanotechnology* **2013**, *24*, 424003. [[CrossRef](#)] [[PubMed](#)]
53. Yin, X.; Li, Y.; Feng, Y.; Feng, W. Polythiophene/graphite fluoride composites cathode for high power and energy densities lithium primary batteries. *Synth. Met.* **2016**, *220*, 560–566. [[CrossRef](#)]
54. Bi, X.; Li, Y.; Qiu, Z.; Liu, C.; Zhou, T.; Zhuo, S.; Zhou, J. Fluorinated graphene prepared by direct fluorination of N, O-doped graphene aerogel at different temperatures for lithium primary batteries. *Materials* **2018**, *11*, 1072. [[CrossRef](#)] [[PubMed](#)]
55. Licht, S.; Wang, B. Nonaqueous phase Fe (VI) electrochemical storage and discharge of super-iron/lithium primary batteries. *Electrochem. Solid-State Lett.* **2000**, *3*, 209. [[CrossRef](#)]
56. Lee, J.-W.; Popov, B.N. Electrochemical intercalation of lithium into polypyrrole/silver vanadium oxide composite used for lithium primary batteries. *J. Power Sources* **2006**, *161*, 565–572. [[CrossRef](#)]

Disclaimer/Publisher's Note: The statements, opinions and data contained in all publications are solely those of the individual author(s) and contributor(s) and not of MDPI and/or the editor(s). MDPI and/or the editor(s) disclaim responsibility for any injury to people or property resulting from any ideas, methods, instructions or products referred to in the content.